PCCP

PAPER

View Article Online
View Journal | View Issue

Cite this: *Phys. Chem. Chem. Phys.*, 2025, **27**, 10235

Hybrid moiré excitons in a strained heterobilayer of transition metal dichalcogenides

Houssem Eddine Hannachi *[a] and Sihem Jaziri[ab]

Received 17th December 2024,
Accepted 10th April 2025

DOI: 10.1039/d4cp04759a

rsc.li/pccp

In this paper, we theoretically investigate the effects of twist and heterostrain on moiré excitons in the $MoSe_2/WSe_2$ heterobilayer. Using a continuum model, we analyze the band structures and wavefunction distributions of moiré excitons, photoluminescence spectra, and the hybridization between interlayer and intralayer moiré excitons. Our key findings reveal that the three-fold rotational symmetry breaking induced by heterostrain leads to significant tunability of the exciton band structure, thereby modifying the distribution of bright-state energies around the light cone. Moreover, tuning the strain magnitude and direction can enhance the brightness of moiré excitons, highlighting the crucial role of strain orientation in excitonic optical modulator applications. Furthermore, the interplay between twist and strain induces a high degree of tunability in the mixing of interlayer and intralayer exciton wavefunctions. Remarkably, under specific strain magnitudes and directions—such as normal compressive strain—we observe the emergence of a topological moiré exciton Chern insulator, characterized by protected edge modes. Our results may pave the way for exploring novel topological exciton phenomena and moiré exciton-correlated physics. They are particularly intriguing for potential device applications with the excitonic quantum anomalous Hall effect (EQAHE) enabled by the combined effects of strain and twist.

1 Introduction

Strain engineering in two-dimensional (2D) materials has emerged as a promising research topic over the last decade.[1–8] Controlling the physical properties of 2D nanomaterials *via* strain remains a subject of great debate due to the complexities involved in its practical implementation. For instance, in experimental setups, errors or uncertainties may arise when strain is applied to the samples, as not all the strain exerted on the substrate can be effectively transferred to the sample.[1,2] From an experimental perspective, strain can be induced by various methods, such as pulling on suspended sheets with an electrostatic gate voltage[3,4] or bending a flexible substrate.[5] Strain effects have been extensively explored in graphene[8–12] and monolayers of transition metal dichalcogenides (TMDs).[3,4,7,13–20] In particular, strain-tuned twisted bilayer systems have garnered significant interest in recent years.[5,6,13,21–25] Twisting bilayers of graphene or TMDs produces a moiré superlattice, which exhibits a three-fold rotational symmetry and is highly sensitive to interlayer deformations. For small interlayer rotation angles, moiré flat bands emerge, playing a crucial role in Bose–Einstein condensation[26,27] and superfluidity[28] phenomena in TMD-based moiré structures. In contrast, the emergence of flat bands in bilayer graphene moiré superlattices—particularly at the so-called magic twist-angle—has been recognised as a promising signature of superconductivity.[29–31] Furthermore, moiré structures based on TMD bilayers provide a rich platform for exploring exotic exciton-correlated physics, such as layer-hybridized moiré excitons.[32–43] In fact, the moiré pattern generates a periodic potential capable of trapping charge carriers, excitons,[44–49] and potentially trions,[42,50] with a strong sensitivity to twist angles. In TMD bilayer systems, excitons are classified as either intralayer (X) or interlayer (IX) excitons, depending on whether the electron and hole reside within the same or different constituent layers. Due to the spatial separation between layers, IXs exhibit weaker light–matter interactions compared to their intralayer counterparts. Moreover, IXs have significantly longer lifetimes, often exceeding 100 nanoseconds, making them promising candidates for exciton condensation phenomena.[27]

Strain-tuned excitons in TMD monolayers have been investigated in various experimental studies.[3,4,7,16,17] For instance, the hybridization of bright and dark excitons has been observed *via* the application of biaxial strain induced by an electrostatic gate voltage in a WSe_2 monolayer,[3,4] yielding a dark exciton valley fingerprinting signature. Additionally, experimental results reported in ref. 7 and 17 suggest that the application of external strain increases the sample temperature, indicating the possibility of exciton–phonon coupling processes. In contrast, to

[a] *Laboratoire de Physique des Matériaux, Faculté des Sciences de Bizerte, Université de Carthage, 7021 Zarzouna, Tunisia.*
E-mail: hannachi.houssemedine@fsb.ucar.tn
[b] *Laboratoire de Physique de la Matière Condensée, Faculté des Sciences de Tunis, Université de Tunis El Manar, 2092 El Manar, Tunisia.*
E-mail: sihem.jaziri@fsb.rnu.tn

the best of our knowledge, strain-modulated excitons in moiré structures remain largely unexplored. However, a theoretical investigation by Zheng *et al.*[21] demonstrated that breaking the three-fold rotational symmetry in moiré exciton wavefunctions, induced by strain in a twisted heterobilayer $WSe_2/MoSe_2$ results in a high degree of tunability of the optical spectra when combined with the twisting effect. Furthermore, it is well established that interlayer coupling (interlayer hopping) induced by twisting can lead to layer hybridization, causing an exchange of symmetries between interlayer and intralayer excitons and giving rise to a new class of excitons with hybrid character. Nevertheless, to the best of our knowledge, the interplay between strain and twist in tuning layer hybridization remains an open question and has yet to be fully explored.

In this work, we theoretically study the miniband dispersion of moiré excitons within a heterostrained $MoSe_2/WSe_2$ heterobilayer. Our study employs an effective continuum model to analyze the moiré exciton band structure, center-of-mass (COM) wavefunctions, photoluminescence (PL) spectra, and layer-hybridized moiré excitons. Inspired by the theoretical framework proposed by Zheng *et al.*,[21] our approach assumes that strain affects only the bottom WSe_2 layer, resulting in an effective gauge field that can shift the Dirac cones. We focus our investigation on the effects of twist and strain at the light cone, where moiré excitons are expected to exhibit bright-state energy distributions. Our main findings include the observation of moiré flat bands in unstrained samples, exhibited by both interlayer and intralayer excitons for small twist angles (less than 2°), consistent with previous studies in the literature. Additionally, we observe both linear and quadratic dependencies of moiré exciton bright-state energies on the twist angle, accompanied by the lifting of degenerate states. However, strain-induced three-fold rotational symmetry breaking leads to significant tunability of the moiré exciton band structure, as well as the underlying bright-state energy distributions, with high adjustability depending on the strain magnitude and orientation. Notably, we observe a topological Chern insulating behavior, characterized by the emergence of protected edge states, when a normal compressive strain is applied. Furthermore, we analyze the degree of hybridization between interlayer and intralayer excitons, revealing a strong sensitivity to the combined effects of twist and strain.

The paper is organized as follows: in Section 2, we develop a detailed theoretical model for moiré excitons within the continuum framework, incorporating the effects of heterostrain. In Section 3, we present our main findings, including the dependence of moiré exciton minibands, COM wavefunctions, and PL spectra on twist angle and strain, as well as the hybridization between interlayer and intralayer excitons. Finally, in Section 4, we summarize our key results.

2. Theoretical framework

2.1. Moiré system

Monolayers of TMDs exhibit a hexagonal lattice structure and feature a direct bandgap at the corners of their hexagonal Brillouin zone (BZ), specifically at the **K** and **K**′ valley points.

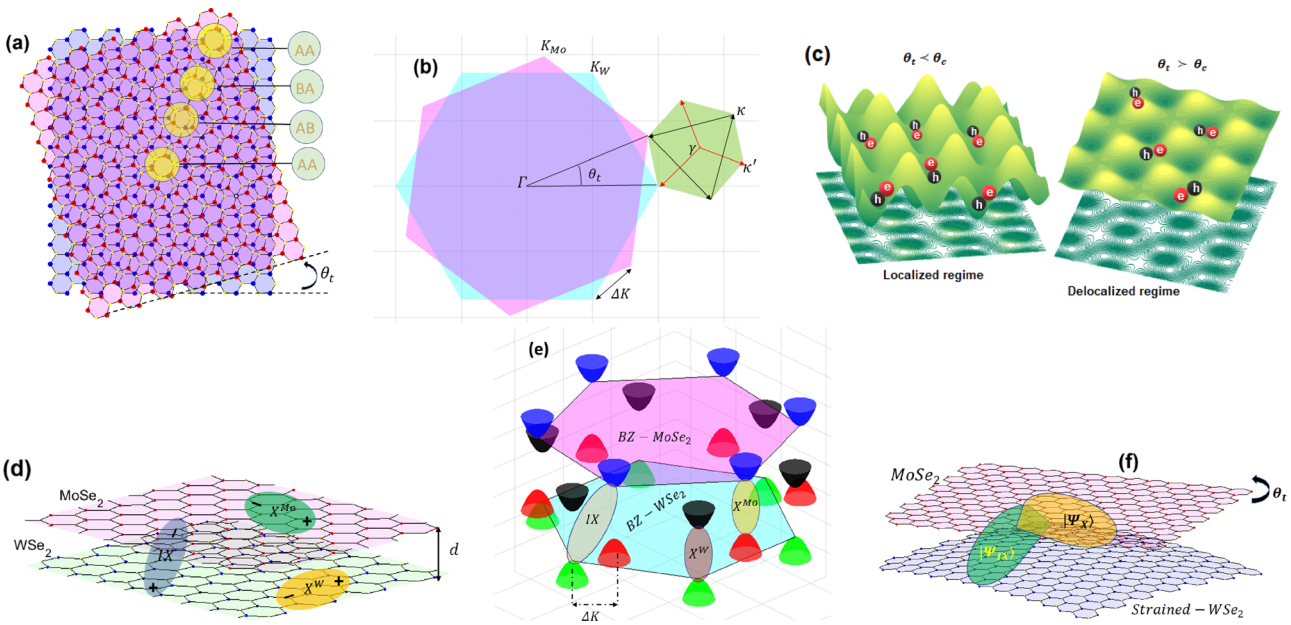

Fig. 1 (a) represents a top view of the twisted $MoSe_2/WSe_2$ heterobilayer, where the yellow circles denote AA, AB, and BA moiré patterns. (b) depicts the formation of the mini Brillouin zone (the green hexagon) due to the stacking of the twisted top and bottom layers' Brillouin zones (the magenta and the cyan hexagons), where the black and red arrows represent the $\mathbf{G}_j$ and $\mathbf{g}(\ell_1,\ell_2)$ moiré vectors in the first mBZ, respectively. (c) depicts the moiré potential, which can confine electron–hole pairs, represented by the red and blue spheres, respectively. Here, the distinction between localized and delocalized regimes is determined by the critical twist angle, θ_c. (d) and (e) illustrate the interlayer exciton (IX) and the intralayer excitons as denoted by $X^{Mo(W)}$, in real and momentum space, respectively. Here, d defines the interlayer separation, the blue (black) and red (green) cones illustrate the conduction and valence bands of the $MoSe_2$ (WSe_2) layer, respectively. The cartoon (f) illustrates the hybridization phenomena between intralayer and interlayer excitons through the combined effects of heterostrain and twist.

When two different monolayers, such as $MoSe_2$ and WSe_2, are vertically stacked, as illustrated in Fig. 1(a), with a slight rotation angle θ_t and/or a lattice mismatch between the layers, periodic moiré patterns emerge. These patterns are characterized by a moiré periodicity given by $a_m = a_{0<}\Big/\sqrt{\theta_t^2 + \delta_0^2}$. Here, $\delta_0 = 1 - a_{0<}/a_{0>}$ represents the lattice mismatch, with $a_{0<(>)}$ denoting the smaller (larger) lattice parameter. For WSe_2 ($MoSe_2$), the lattice parameters are a_0 = 3.299 (3.286), respectively.[41,46]

This moiré network is characterized by three distinct atomic registries, denoted as AA, AB and BA stackings, which are related through the three-fold rotational symmetry, C_{3z}. AA stacking refers to a hexagonal registry in which the transition metal atoms of the $MoSe_2$ layer are aligned directly on top of the transition metal atoms of the WSe_2 layer. In contrast, the AB and BA stackings exhibit a lateral shift between the two layers, where the transition-metal atoms of one layer align directly with the chalcogen atoms of the other layer. These two atomic configurations are determined by the rotational symmetries C_{3z}^1 and C_{3z}^2 with respect to the AA stacking, respectively.

In addition, the slight interlayer rotation between the two layers introduces a valley mismatch in momentum space, characterized by the vector $\Delta K = \tau\mathbf{K}_W - \tau'\mathbf{K}_{Mo}$, where $\tau(\tau') = \pm 1$ represents the two-fold valley degeneracy of the WSe_2 ($MoSe_2$) layer. In our investigation, we only consider the +(+) valley indices. This valley mismatch gives rise to an effective mini-Brillouin zone (mBZ), represented by the green hexagon in Fig. 1(b), which features high-symmetry points denoted as κ, γ, and κ'. It is important to note that the twist angle is defined by rotating the top layer ($MoSe_2$). For small twist angles, the valley mismatch can be approximated as $\Delta\mathbf{K} \simeq \theta_t\mathbf{K}_W$, where the magnitude of the Dirac point is $\mathbf{K}_W = 4\pi/3a_0$.

The mBZ can be experimentally visualized using photoemission spectroscopy, as demonstrated in the work of Bange *et al.*[51] on the WSe_2/MoS_2 heterobilayer. Their study revealed that the γ point aligns with the $\mathbf{K}_W$ valley of the WSe_2 monolayer, while the edge corners $\kappa(\kappa')$ coincide with the $\mathbf{K}_{Mo}$ valley of the MoS_2 monolayer.

The interlayer twist angle not only induces relative shifts in momentum space but also profoundly affects the real-space moiré pattern. This gives rise to a spatial modulation in the band-gap energy, a defining feature known as the moiré potential. As depicted in Fig. 1(c), this potential creates periodic energy landscapes capable of trapping excitons. It can be mathematically expressed as:[48,49]

$$V_M(\boldsymbol{R}) = V_0 \sum_{j=1}^{6} e^{i\left(\boldsymbol{G}_j\boldsymbol{R} + \psi_0\right)}. \quad (1)$$

Here, V_0 and ψ_0 represent the moiré potential amplitude and a characteristic phase, respectively. These parameters are material-dependent and vary between different stacking configurations and atomic registries. Their values can be obtained from DFT calculations. Specifically, we expect them to be approximately 9 meV and 0.57π for R-stacking (where the two layers share the same orientation), consistent with existing literature.[21] We define $\mathbf{R}$ as the in-plane real-space vector on the moiré superlattice. The studied heterobilayer exhibits a three-fold rotational symmetry, with displacements on the moiré superlattice vector given by: $\mathbf{R} = N(\mathbf{a}_1 + \mathbf{a}_2)/3$.[48] Here, N is an integer number, where $N = 0$ for the AA stacking and N = 1,2 for the AB and BA stackings, respectively. a_1 and a_2 represent the primitive vectors of the moiré superlattice, satisfying $\mathbf{a}_i = a_m\left(\sin\left(\frac{2\pi(i-1)}{3}\right), \cos\left(\frac{2\pi(i-1)}{3}\right)\right)$, with the integer i = 1, 2, 3. We can deduce the moiré wave vectors using the reciprocal relationship $\mathbf{a}_i\cdot\mathbf{G}_j = 2\pi\delta_{ij}$, and find then $\mathbf{G}_j = k_\theta\left(\cos\left(\frac{2\pi(j-1)}{3}\right), \sin\left(\frac{2\pi(j-1)}{3}\right)\right)$,[13] with $k_\theta = 4\pi/\sqrt{3}a_m$. In addition to the first-shell reciprocal lattice vectors, $\mathbf{G}_j$, we define another set of moiré vectors in terms of the $\mathbf{G}_j$ vectors, connecting the γ point to the $\kappa(\kappa')$ points, as follows:[32,42,43] $\mathbf{g}(\ell_1,\ell_2) = (\ell_1\mathbf{G}_1 + \ell_2\mathbf{G}_2)/\sqrt{3}$, where ℓ_1 and ℓ_2 are integers. In Fig. 1(b), the moiré vectors $\mathbf{G}_j$ and $\mathbf{g}(\ell_1,\ell_2)$ are depicted in the first mBZ by black and red arrows, respectively. These moiré vectors are of significant interest in defining the moiré exciton's wavefunction and, consequently, in determining its corresponding band structure over the mBZ. This intriguing role will be introduced and elaborated upon in the subsequent parts of this paper.

2.2 Moiré excitons Hamiltonian

Photoluminescence experimental results have shown that TMD bilayer systems are predominantly influenced by both intralayer and interlayer exciton signatures.[37,43] These two types of excitons are distinguished based on whether the electron and hole reside within the same or different constituent monolayers. Fig. 1(d) and (e) illustrate the IX and intralayer excitons, denoted as $X^{W(Mo)}$, in the real and momentum space, respectively. These moiré excitons, which are electron–hole pairs interacting *via* Coulomb forces, are described within the framework of the Rytova–Keldysh model.[52,53] Considering the moiré translation vector $\mathbf{g}$, the moiré excitons can be adequately represented using the eigenstate basis:[21,34,41,50]

$$\langle \mathbf{r}, \mathbf{R} | n, m; \mathbf{Q} + \mathbf{g}\rangle = \boldsymbol{\phi}_{n,m}(r) e^{-i(\mathbf{Q}+\mathbf{g})\mathbf{R}}\Big/\sqrt{S}. \quad (2)$$

Here, $\mathbf{Q} = \mathbf{K}_c - \Delta K$ defines the COM exciton momentum, also referred to as the kinetic momentum. This is relevant only for interlayer excitons, while ΔK is neglected from the COM momentum in the case of intralayer excitons ($\mathbf{Q} \sim \mathbf{K}_c$). The term $\mathbf{K}_c$ represents the crystal momentum, expected to be the sum of the electron and hole momenta, satisfying $\mathbf{K}_c = \sum_{\alpha=e,h} k_\alpha$, where $\mathbf{k}_{e(h)} = \pm\mathbf{q} + \mathbf{K}_c m_{e(h)}/M_X$. Here, the subscript α denotes the electron (e) and the hole (h), and $\mathbf{q}$ represents the internal exciton momentum. The COM coordinates are defined as $R = \sum_{\alpha=e,h} m_\alpha r_\alpha / M_X$, where $M_X = m_e + m_h$ is the total exciton mass, in terms of the individual band masses of the electron and hole. The term S represents the area of the unit cell of the moiré superlattice, while $\phi_{n,m}(r)$ is the two-dimensional hydrogen-like wavefunction, expressed in terms of the

magnitude of the in-plane exciton internal motion vector $r = |\mathbf{r}_e - \mathbf{r}_h|$. This wavefunction is a solution to the internal motion Hamiltonian and is associated with eigenvalues $E_{n,m} = \Delta - E^b_{n,m}$. Here, Δ is the bandgap energy, and $E^b_{n,m}$ defines the exciton binding energy, where the indices n and m denote the principal and angular momentum quantum numbers, respectively. Within this eigenstate basis, the Hamiltonian matrix for the moiré excitons reads

$$\langle n,m;\mathbf{Q}+\mathbf{g}|\mathbf{H}|n',m';\mathbf{Q}+\mathbf{g}'\rangle = \left\{E_{n,m}+\frac{\hbar^2|\mathbf{Q}+\mathbf{g}|^2}{2M_X}\right\}\delta_{n,n'}\delta_{m,m'}\delta_{\mathbf{g},\mathbf{g}'} + \sum_{j=1}^{6} V_0 e^{i\psi_0}\delta_{n,n'}\delta_{m,m'}\delta_{\mathbf{g}-\mathbf{g}',\mathbf{G}_j} + \text{h.c.} \quad (3)$$

It should be noted that, in our calculations, we consider only the 1s Rydberg state with the corresponding eigenvector expressed as $\varphi_{1s}(r) = \sum_{n,m} D_{n,m}\phi_{n,m}(r)$. The coefficients $D_{n,m}$ are obtained from the numerical diagonalization of the exciton internal motion Hamiltonian.[54–56] This approach yields the ground-state exciton eigenvalues within an hBN/$MoSe_2$/WSe_2/hBN heterostructure as E_{1s} = 1.42 eV, 1.56 eV, and 1.67 eV, corresponding to the IX, X^{Mo}, and X^{W} excitons, respectively. These values are determined based on the bandgap energies Δ = 1.52 eV, 1.72 eV, and 1.84 eV for the WSe_2/$MoSe_2$ heterobilayer, $MoSe_2$, and WSe_2 monolayers, respectively. Additionally, we use the effective masses of charge carriers within the $MoSe_2$ (WSe_2) monolayers: m_e = 0.8(0.5) and m_h = 0.5(0.45), expressed in units of the free electron mass, m_0.[41,46] Further details on the resolution of the internal motion Hamiltonian for interlayer and intralayer excitons, as well as the dependence of interlayer exciton binding energy spectra on the dielectric environment and interlayer separation, are provided in our previous works.[54–56]

Another approximation is introduced in eqn (3), assuming that the exciton moiré potential can be expressed as the sum of the electron and hole moiré potentials, with dependencies on both the internal and COM coordinates. In the limit of a large moiré period, the exciton moiré potential can be expanded

$$V_M(\mathbf{r},\mathbf{R}) = \sum_{\alpha=e,h} V^{\alpha}_M\left(\mathbf{R}\pm\frac{m_{h(e)}}{M_X}\mathbf{r}\right) \simeq \sum_{\alpha=e,h}\left(V^{\alpha}_M(\mathbf{R})\pm\frac{m_{h(e)}}{M_X}\mathbf{r}\nabla_{\mathbf{R}}RV^{\alpha}_M(\mathbf{R})\right)\simeq V_M(\mathbf{R}), \quad (4)$$

here, the term $\langle \mathbf{r}\nabla_{\mathbf{R}}V^{\alpha}_M(\mathbf{R})\rangle \propto a_B/a_m$, where $a_B \sim$ 1–2 nm is the exciton Bohr radius and $a_m \sim$ 50–100 nm is the moiré period, yielding $a_B/a_m \ll 1$. We also assume that the potential amplitude satisfies $V_0 = V^e_0 + V^h_0$. Under these approximations, the internal and COM motions of the moiré exciton can be safely decoupled. Consequently, the exciton moiré potential is considered to depend solely on the COM coordinate.

An intriguing point worth emphasizing is that when an exciton is converted into a photon, momentum conservation requires the crystal momentum to satisfy $\mathbf{K}_c \sim 0$. As a result, the bright-state energy of moiré IXs emerges at a finite kinetic momentum, $\mathbf{Q}_0 \sim \Delta K$, whereas the bright-state energy of intralayer excitons aligns with $\mathbf{Q}_0 \sim 0$. The kinetic momentum $\mathbf{Q}_0$ determines the position of the light cone for moiré excitons, which is expected to be centered around the γ point of the mBZ. Remarkably, the moiré system also exhibits Umklapp light cones, stemming from the periodicity and three-fold rotational symmetry of the moiré superlattice. The Umklapp scattering process involves momentum transfer between the first mBZ and adjacent mBZs, facilitated by the moiré reciprocal lattice vectors $\mathbf{G}_j$ and $\mathbf{g}(\ell_1,\ell_2)$. For instance, the light cones in the second mBZ can be identified by translating the γ point of the first mBZ *via* $\mathbf{G}_j$, while translating $\kappa(\kappa')$ using $\mathbf{g}(\ell_1,\ell_2)$ determines the edge corners of the second mBZ.

2.3 Layer-hybridized moiré excitons

In this subsection, we discuss the hybridization between interlayer and intralayer moiré excitons in a twisted TMD bilayer system. In general, twisting the layers introduces a moiré superlattice, which modifies the electronic band structure and facilitates electron (hole) tunneling between the conduction (valence) bands of the WSe_2 and $MoSe_2$ layers. This process is governed by an interlayer hopping term, which can be expressed in terms of the moiré reciprocal lattice vectors,[32,41–43]

$$T(\mathbf{R}) = t_0\left(1 + e^{i\mathbf{G}_1\cdot\mathbf{R}} + e^{i\mathbf{G}_2\cdot\mathbf{R}}\right),$$

here, t_0 represents the interlayer hopping amplitude, which can be theoretically determined using DFT calculations. According to the literature,[6,32,37,41] its energy scale ranges from approximately 10 to 30 meV for the studied (or similar) heterobilayer systems. Based on these references, we adopt a moderate value of t_0 = 15 meV in our investigation. This tunneling term plays a crucial role in coupling the two layers, potentially inducing significant overlap between the wavefunctions of interlayer and intralayer excitons.

Within this framework, we anticipate the hybridization of IX with X^{Mo} due to interlayer hopping, which can be formally described by the following Hamiltonian

$$H_h = \begin{pmatrix} H_{IX} & T \\ T^* & H_X \end{pmatrix}. \quad (5)$$

Here, H_{IX} and H_X are the moiré interlayer and intralayer exciton Hamiltonians as defined in eqn (3), respectively. In counterpart, the interlayer hopping matrix element may read as[32,42,43]

$$\langle \mathrm{IX};\mathbf{Q}'+\mathbf{g}'|T|\mathrm{X};\mathbf{Q}+\mathbf{g}\rangle = t_0\{\delta_{\mathbf{Q}+\mathbf{g},\mathbf{Q}'+\mathbf{g}'} + \delta_{\mathbf{Q}+\mathbf{g},\mathbf{Q}'+\mathbf{g}'+\mathbf{G}_1} + \delta_{\mathbf{Q}+\mathbf{g},\mathbf{Q}'+\mathbf{g}'+\mathbf{G}_2}\}. \quad (6)$$

This term facilitates the mixing of wavefunctions between the two distinct excitons, leading to the formation of hybrid states. These hybridized states are expected to exhibit distinct signatures in photoluminescence spectra, reflecting the interplay between the moiré potential and interlayer interactions.

2.4 Heterostrain perturbation effects

The three-fold rotational symmetry in the studied heterobilayer system can be broken by substrate-induced or externally applied strain. Symmetry breaking due to strain has been observed in previous studies.[8,21] Notably, the physical properties of twisted heterobilayers primarily depend on the relative deformation between the two layers. In this work, we consider heterostrain applied exclusively to the bottom layer WSe_2, while the top layer $MoSe_2$ is assumed to remain strain-free. In general, strain is defined as the ratio of relative deformation (change in length, area, or volume) to the original dimensions of the material. Specifically, it can be extended to a two-dimensional tensor form as

$$\varepsilon_s = \begin{pmatrix} \varepsilon_{xx} & \varepsilon_{xy} \\ \varepsilon_{yx} & \varepsilon_{yy} \end{pmatrix}. \tag{7}$$

This matrix captures different types of strain, including:

• Uniaxial strain: only one diagonal component is non-zero, while the off-diagonal components remain zero. This represents stretching (tensile) or compression along a single axis, depending on whether the strain magnitude is positive or negative, respectively.

• Biaxial strain: represents uniform tensile or compression in both the x- and y-directions. The off-diagonal components are zero, and the strain is isotropic when $\varepsilon_{xx} = \varepsilon_{yy}$.

• Normal compression: a specific type of biaxial strain where $\varepsilon_{xx} = -\varepsilon_{yy}$ and $\varepsilon_{xy} = \varepsilon_{yx} = 0$. This indicates simultaneous elongation along one axis and compression along the perpendicular axis.

• Shear strain: characterized by angular deformation without any length change along the principal axes. In this case, only the off-diagonal components (ε_{xy} and ε_{yx}) are non-zero.

Beyond the general form of the homogeneous strain tensor (eqn (7)), the tensor can be extended to account for more complex systems where the strain direction is characterized by an angle ϕ_s. This angle defines the orientation of the stretching direction relative to the x-axis, describing what is known as anisotropic in-plane strain or generalized uniaxial strain. In this case the strain tensor is expressed in the following form:[8,13]

$$\varepsilon_s = \mathbf{R}(\phi_s)^{-1} \begin{pmatrix} -\varepsilon_0 & 0 \\ 0 & \nu\varepsilon_0 \end{pmatrix}$$

$$\mathbf{R}(\phi_s) = \varepsilon_0 \begin{pmatrix} \cos(\phi_s)^2 - \nu\sin(\phi_s)^2 & (1+\nu)\cos(\phi_s)\sin(\phi_s) \\ (1+\nu)\cos(\phi_s)\sin(\phi_s) & \sin(\phi_s)^2 - \nu\cos(\phi_s)^2 \end{pmatrix}. \tag{8}$$

Here, $\mathbf{R}(\phi_s)$ is the rotation matrix, ε_0 defines the strain magnitude and $\nu = 0.19$ is the Poisson ratio for the WSe_2 layer,[13,57] which captures the transverse response when the material is stretched or compressed. This strain form satisfies that the trace of the strain tensor, $\mathrm{Tr}(\varepsilon_s) = \varepsilon_s(1-\nu)$, indicating that the strain changes the material's area or volume.

In some case, the strain is isochoric (incompressible), which is so-called volume-preserving strain, in which the material's volume remains constant under deformation. Mathematically this means that the trace of the strain tensor, $\mathrm{Tr}(\varepsilon_s) = \varepsilon_{xx} + \varepsilon_{yy} = 0$. Here, the strain effect is dominated by the off-diagonal terms, which implies that any expansion in one direction is exactly compensated by compression in the perpendicular direction, maintaining the overall volume or area. In this case, the strain tensor is given by:[8,21]

$$\varepsilon_s = \varepsilon_0 \begin{pmatrix} \cos(\phi_s) & \sin(\phi_s) \\ \sin(\phi_s) & -\cos(\phi_s) \end{pmatrix}. \tag{9}$$

Geometrically, a deformation ε_s alters both the shape of the unit cell and the corresponding Brillouin zone. Mathematically, for small strain magnitudes, the rescaled primitive and reciprocal lattice vectors are given by[8]

$$\mathbf{a}_i^s \simeq (1+\varepsilon_s)\mathbf{a}_i \text{ and } \mathbf{G}_j^s \simeq \left(1-\varepsilon_s^T\right)\mathbf{G}_j, \tag{10}$$

here, the term 1 is the identity matrix. In addition to the geometric effect, the strain shifts the Dirac cones for bottom layer WSe_2 to

$$\mathbf{K}_S = \left(1-\varepsilon_s^T\right)\mathbf{K}_W - \tau\mathbf{A}, \tag{11}$$

and generating an effective gauge field

$$\mathbf{A} = \frac{\sqrt{3}}{2a_0}\beta(\varepsilon_{xx} - \varepsilon_{yy}, -2\varepsilon_{xy}), \tag{12}$$

with β is due to the strain dependence of the in-plane hopping parameters and estimated to be 2.30 for the WSe_2 monolayer according to the previous first principal calculation.[8,21] Consequently, a continuum moiré exciton Hamiltonian in a heterostrained $MoSe_2/WSe_2$ heterobilayer is obtained by replacing the kinetic energy (second term in eqn (3)) as:[8,13]

$$E_{\mathbf{Q}_s} \simeq \frac{\hbar^2}{2M_X}\left(\left(1+\varepsilon_s^T\right)(\mathbf{Q}+\mathbf{g}-\mathbf{K}_S)\right)^2. \tag{13}$$

It is worth noting that the strain-induced shifting of the Dirac cones should be smaller than the valley mismatch, given by $|\Delta K| \sim \frac{4\pi}{3a_m}$. To illustrate this, we consider a strain strength in the range of 0.5% to 2% to assess its impact on moiré excitons.

We also emphasize that our study focuses exclusively on K–K IXs and their hybridization with intralayer excitons, X^{Mo}, while considering the contribution of other types of IXs, such as those forming in the K–Γ and K–Q valleys, to be negligible. Indeed, in the absence of external perturbations or defects in the TMD bilayer (*e.g.*, electric fields, magnetic fields, phonons, or strain) and for small twist angles between the layers, K–K IXs are expected to be optically bright in the PL spectra, whereas K–Γ and K–Q IXs remain dark. In fact, the K–K IXs, involving electron and hole states from the K valleys of both layers, experience a small valley mismatch $\Delta\mathbf{K}$, allowing them to efficiently couple with light and thus appear as bright excitons. In contrast, K–Γ and K–Q IXs exhibit larger momentum mismatches, preventing direct radiative recombination. Moreover, spin-valley selection rules impose additional constraints

on the allowed optical transitions, reinforcing the dark nature of these excitons. Although strain can break the three-fold rotational symmetry of the moiré superlattice—possibly inducing hybridization between bright K–K IXs and dark K–Γ or K–Q IXs, thereby endowing the latter with oscillator strength and rendering them optically active–we do not consider these effects in the present work.

3 Results and discussion

In this section, we first present our results without incorporating strain effects, focusing solely on the twist-angle dependence of moiré excitons. In the next step, we introduce the heterostrain effect and analyze its impact on moiré exciton minibands, wavefunction distributions, and PL spectra. Finally, we explore the degree of the hybridization between interlayer and intralayer excitons under the combined influence of twist and heterostrain effects.

3.1 Twist angle dependence of moiré exciton mini-bands, wavefunction distributions and PL spectra

We determined the excitonic band structure for an unstrained twisted $MoSe_2/WSe_2$ heterobilayer encapsulated in hBN, as shown in Fig. 2. This figure displays the minibands of moiré IX and X^{Mo} at 1° and 3° twist-angles, respectively. The band structures are obtained through numerical diagonalization of the moiré exciton Hamiltonian presented in eqn (3), using a matrix size of 81×81. The Hamiltonian size is determined by employing a moderate truncation order of $\ell_0 = 4$, which we find sufficient to ensure convergence of the calculations. Physically, this corresponds to considering up to the fourth Umklapp light cones (or mBZ). The band structures are plotted for AA patterns along a high-symmetry path of the hexagonal mBZ, with the center around the light cone (γ point) and the edges at $\kappa(\kappa') = \pm\Delta\mathbf{K}$.

At a 1° twist angle, both interlayer and intralayer excitons exhibit clearly flat band dispersions, as depicted in Fig. 2(a) and (c), respectively. This behavior arises from the deeper moiré potential at small twist angles, which acts similarly to a parabolic quantum dot, localizing the moiré exciton states and resulting in the observed flat bands. In contrast, at a 3° twist angle, the moiré interlayer and intralayer excitons display nearly parabolic band dispersions, as shown in Fig. 2(b) and (d). This transition is due to the delocalization of states induced by the moiré potential at larger twist angles, resulting in delocalized scattering states. This can be understood by the decreased moiré period and, consequently, the reduction in the moiré potential size. Within the harmonic approximation, the size of the moiré potential, R_m, can be expressed in terms of the moiré period as $R_m \sim \sqrt{l_m a_m}$, where l_m is a characteristic length on the order of a few Ångströms.[54,55]

In Fig. 3(a) and (b), we show the twist angle dependence of the first eigenvalues of moiré interlayer and intralayer excitons around the light cone, respectively. The variation in bright-state energies exhibits two distinct trends. For small twist angles ($\theta_t < 2°$), the energies of the bright states increase linearly with the twist angle θ_t. This behavior is due to the localization of states in the regime of a large moiré period, as previously discussed. Conversely, for larger twist angles ($\theta_t > 2°$), the excited states display a quasi-quadratic increase in energy with respect to the twist angle, reflecting the fact that the kinetic momentum evolves as $|Q|^2 \sim \theta_t^2$. This indicates that the states become delocalized as the moiré period decreases. This can be understood by the presence of a critical twist angle $\theta_c \simeq 2°$. Around this specific angle, localized states emerge for $\theta_t < \theta_c$, while delocalized scattering states appear for $\theta_t > \theta_c$ (as illustrated in Fig. 1(c)).

Additionally, within this quadratic regime, we observe a lifting of the COM degeneracy of states, as highlighted by the red circle in Fig. 3(a). This can be understood as a consequence of increasing twist angle, which induces trigonal distortions in the moiré potential, breaking its circular symmetry and lifting the degeneracy of initially doubly degenerate states. Furthermore, we identify an avoided crossing between excited states, which may lead to hybridization between states in adjacent minima of the moiré potential, resulting in states mixing that inherits different symmetries. Notably, the lowest bright-state energy of the IX continues to increase linearly with respect to

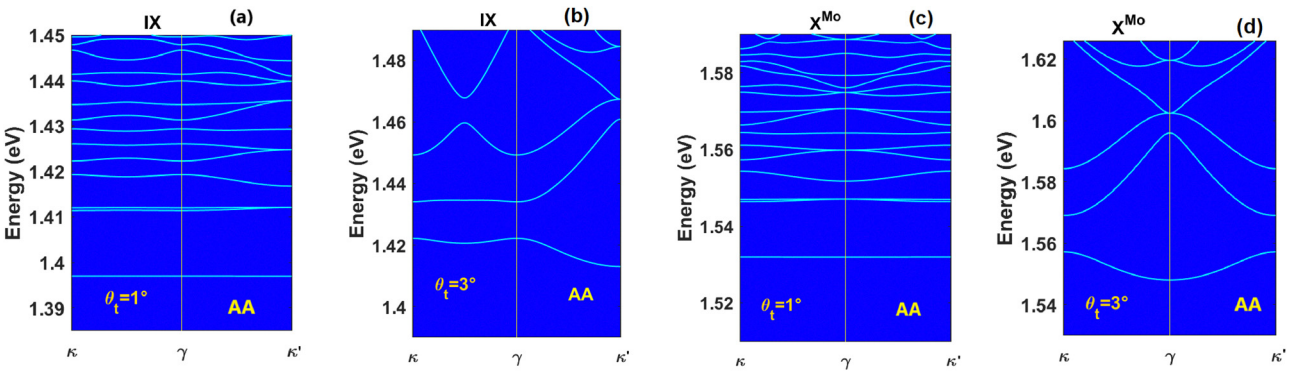

Fig. 2 Interlayer and intralayer exciton band structures within an unstrained R-$MoSe_2/WSe_2$ heterobilayer encapsulated in hBN. (a) and (b) correspond to IX for twist-angle $\theta_t = 1°$ (a) and $\theta = 3°$ (b), respectively. (c) and (d) are the band structures of intralayer exciton X^{Mo}. (c) for $\theta_t = 1°$, (d) for $\theta_t = 3°$, respectively. The yellow vertical line represents the light cone, indicating that only the states near the γ point are expected to couple directly to the light.

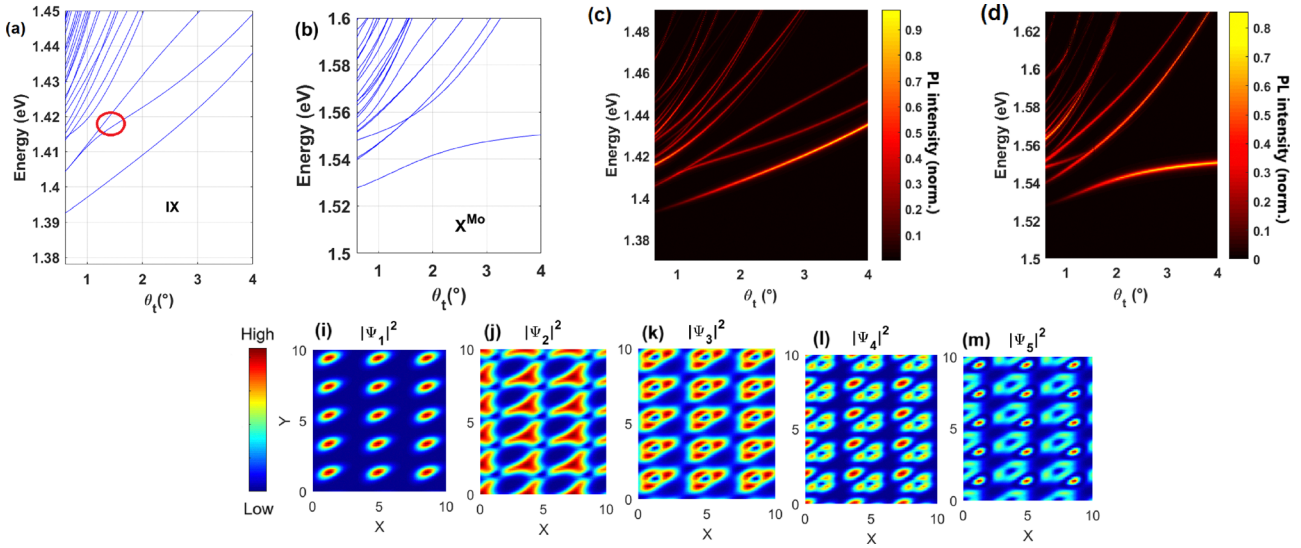

Fig. 3 (a) and (b) show the dependence of the bright-state energies on the twist-angle for IX and X^{Mo} moiré excitons, respectively. Here, the red circle highlights the lifting of state degeneracy. We also note that other excited states remain degenerate at small twist angles, while this degeneracy is lifted as the twist angle increases. This degeneracy breaking can be understood as follows: for small twist angles, the moiré potential minima is very wide, allowing for states that exhibit nearly circular symmetry. In this regime, excited states that inherit a nonzero angular momentum symmetry are doubly degenerate. As the twist angle increases, the moiré potential develops trigonal distortions that break its circular symmetry, thereby lifting the degeneracy between angular momentum states. (c) and (d) illustrate the PL map dependence on the twist-angle effect for IX and X^{Mo} moiré excitons, respectively. (i–m) are the first IX's density of states $|\Psi_\ell(R)|^2$, taken for a twist angle $\theta_t = 3^\circ$.

the twist angle, in contrast to the intralayer exciton, which exhibits a quadratic increase in energy in the higher twist-angle regime. This behavior can be understood by considering the indirect nature of the IX in a twisted heterobilayer. The bright-state energy resonance of the IX is situated around $\mathbf{Q} \sim \Delta\mathbf{K}$, whereas the intralayer exciton resonance is centered at $\mathbf{Q} \sim 0$.

In Fig. 3(c) and (d), we present the PL map illustrating the dependence of interlayer and intralayer excitons on the twist angle. The excitonic states exhibit a blue shift with increasing twist angle, indicating an enhancement in the brightness of the ground-state energy. However, for the highest excited states, we observe a noticeable decrease in brightness with increasing twist angle, accompanied by an increasing energy splitting between neighboring states. These PL spectra were determined using the Lorentzian formula:

$$I_{\mathrm{PL}}(\hbar\omega_{\mathrm{ph}}) \sim f^{\mathrm{osc}}_{1\mathrm{s},\ell} \frac{\Gamma_0}{\pi\left(\hbar\omega_{\mathrm{ph}} - E^{1\mathrm{s}}_{\ell}\right)^2 + \Gamma_0{}^2}, \tag{14}$$

here, $\hbar\omega_{\mathrm{ph}}$ is the photon excitation energy, $E^{1\mathrm{s}}_{\ell}$ is the moiré exciton energy and Γ_0 is the broadening energy which we set to be approximately 10 meV. The term $f^{\mathrm{osc}}_{1\mathrm{s},\ell}$ defines the oscillator strength of moiré excitons states $|1\mathrm{s};\mathbf{K}_c = 0,\mathbf{g}\rangle$, which is read in terms of the optical matrix element as:

$$f^{\mathrm{osc}}_{1\mathrm{s},\ell} \sim \sum_{\ell} \frac{m_0\Delta}{m_e E^{1\mathrm{s}}_{\ell}} |\varphi_{1\mathrm{s}}(r=0)|^2 \left| \int_0^{\infty} \Psi_\ell(R) \mathrm{d}^2R \right|^2. \tag{15}$$

The COM eigenvectors, expressed in terms of the plane wavefunction as $\Psi_\ell(R) = \sum_\ell C_\ell e^{-i\mathbf{g}\cdot\mathbf{R}} \Big/ \sqrt{S}$, are also determined in this work. Here, C_ℓ represents the coefficient obtained through numerical diagonalization, and ℓ denotes the quantum number. Fig. 3(i–m) shows the spatial densities of the first five IX eigenvectors around the light cone at a 3° twist angle. The three-fold rotational symmetry is evident in the spatial distribution of the excited states. The lowest-energy state exhibits s-type symmetry, while the remaining states inherit p-type symmetry.

Our results are consistent with previous works in the literature. For instance, we find a good agreement with the theoretical study conducted by Brem *et al.*,[44] where the authors analyzed the twist-angle dependence of both interlayer and intralayer excitons, including their miniband dispersions, wavefunctions, and optical absorption spectra. They employed a combination of first-principles calculations and the excitonic density matrix formalism for the $MoSe_2/WSe_2$ bilayer. Our findings regarding the excitonic band structure (Fig. 2), the twist-angle dependence of excitonic bright-state energies around the light cone, and related results such as wavefunctions and PL spectra (Fig. 3), align well with this reference. Additional studies[21,33,37,38,45,48] that utilized an effective continuum model for similar bilayer systems also provide further avenues for comparison and validation.

3.2. Heterostrain modulates the moiré exciton mini-band dispersion, wavefunctions and optical spectra

In Fig. 4, we present the band structure of IX within a hetero-strained $MoSe_2/WSe_2$ heterobilayer, considering a fixed twist angle of 3° and an AA-stacking configuration. Fig. 4(a–c) illustrate the effects of homogeneous uniaxial, biaxial, and normal compressive strain, respectively. For uniaxial and biaxial strain, the bands exhibit a blueshift as the strain magnitude increases from 0.5% to 1%. Interestingly, in the case of normal compressive strain, a 0.5% strain magnitude induces a quasi-flat

band for the lowest-energy state, consistent with previous studies.[8,11,58] However, when the normal compressive strain strength is increased to 1%, highly correlated bands emerge, exhibiting characteristics of a Chern insulator, as indicated by the presence of protected edge states. Indeed, strain has been reported to highlight interlayer exciton-protected edge modes, as discussed in ref. 22. Moreover, strain-induced topological phase transitions have recently been observed in Janus monolayers.[59]

To further explore the topological nature of these bands, we perform a detailed topological analysis. In particular, bands can be classified as either topologically trivial or nontrivial based on their Chern number, a topological invariant that distinguishes between different band topologies. A Chern number of zero corresponds to a trivial band, whereas a nonzero Chern number indicates a nontrivial topological band, characterized by the presence of robust edge states. Physically, the Chern number is defined as the integral of the Berry curvature over the mBZ, which may read as

$$C_\ell = \frac{1}{2\pi}\int_{\mathrm{mBZ}} \Omega_\ell(\mathbf{k})\mathrm{d}^2\mathbf{k}, \tag{16}$$

where

$$\boldsymbol{\Omega}_\ell(\mathbf{k}) = 2i\sum_{\ell\neq\ell'} \frac{\left\langle \Psi_\ell(\mathbf{R})\left|\frac{\partial H}{\partial k_x}\right|\Psi_{\ell'}(\mathbf{R})\right\rangle\left\langle \Psi_{\ell'}(\mathbf{R})\left|\frac{\partial H}{\partial k_y}\right|\Psi_\ell(\mathbf{R})\right\rangle}{\left(E_\ell(\mathbf{k}) - E_{\ell'}(\mathbf{k})\right)^2}, \tag{17}$$

is the Berry curvature of the Bloch states, which describes interband coupling and is derived using perturbation theory.

In Fig. 5(a), we present the IX band structure with the corresponding normalized Berry curvature distribution projected onto the bands for a 0.5% strength of normal compressive strain. Meanwhile, Fig. 5(b) illustrates the distribution of the normalized Berry curvature for the first six bands along the high-symmetry path κ–γ–κ' in the mBZ. We observe that the lowest two bands exhibit a noticeable Berry curvature resonances across the mBZ. In contrast, the excited states, particularly the third and fourth bands, display singularities in the Berry curvature distribution, where the Berry curvature is significantly nonzero only near the band anticrossings. In Fig. 5(c), we numerically evaluate the Chern numbers for the lowest energy bands. Our calculations reveal that the two lowest bands are topologically trivial with a Chern number of zero, whereas the third to sixth bands are topologically nontrivial, carrying nonzero Chern numbers. This indicates the emergence of topologically protected edge states, which may be understood as a consequence of strain-induced time-reversal symmetry breaking. These findings are particularly promising for potential applications in excitonic quantum anomalous Hall effect (EQAHE) devices.

We also investigate the effects of volume-preserving strain, as shown in Fig. 4(d–f). Fig. 4(d) corresponds to a strain direction of $\phi_s = 0^\circ$, which is consistent with the normal compressive strain case presented in Fig. 4(c). Fig. 4(e) and (f) illustrates strain directions of $\phi_s = 30^\circ$ and $\phi_s = 45^\circ$, respectively. In these cases, we observe a redshift in the energy bands, further highlighting

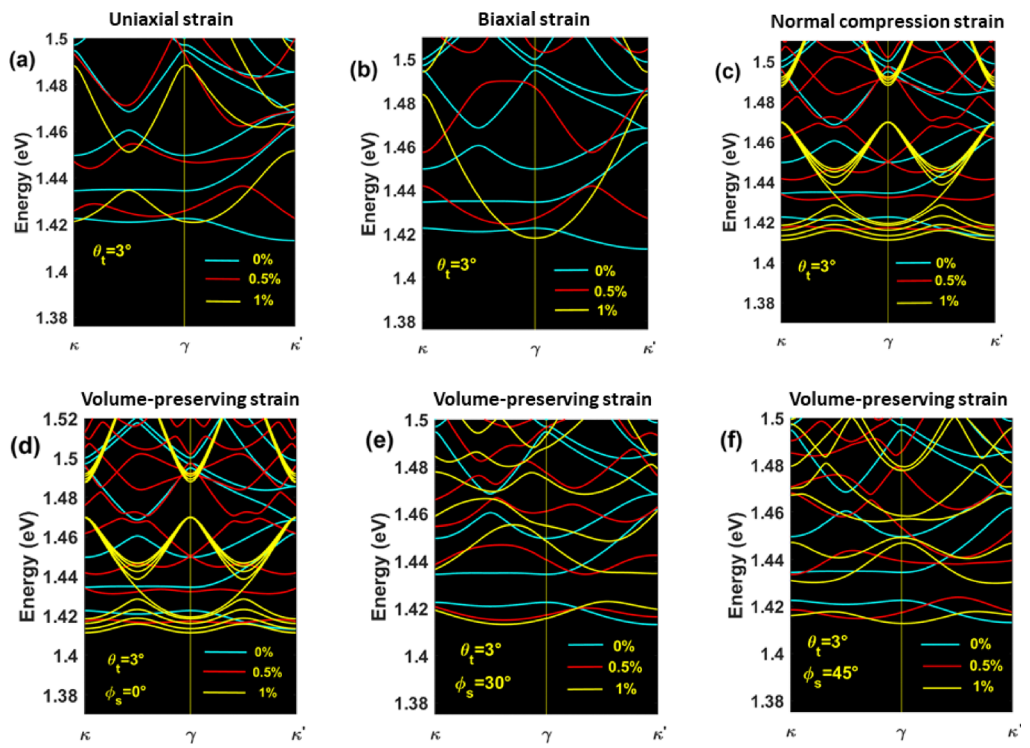

Fig. 4 Moiré interlayer exciton band structure dependence on the strain effect, for AA pattern and fixed twist-angle $\theta_t = 3^\circ$. (a)–(c) Uniaxial, biaxial and normal compression strain effects, respectively. (d)–(f) Volume-preserving strain dependence taken for different values of the strain direction angle, ϕ_s = 0°, 30° and 45°, respectively.

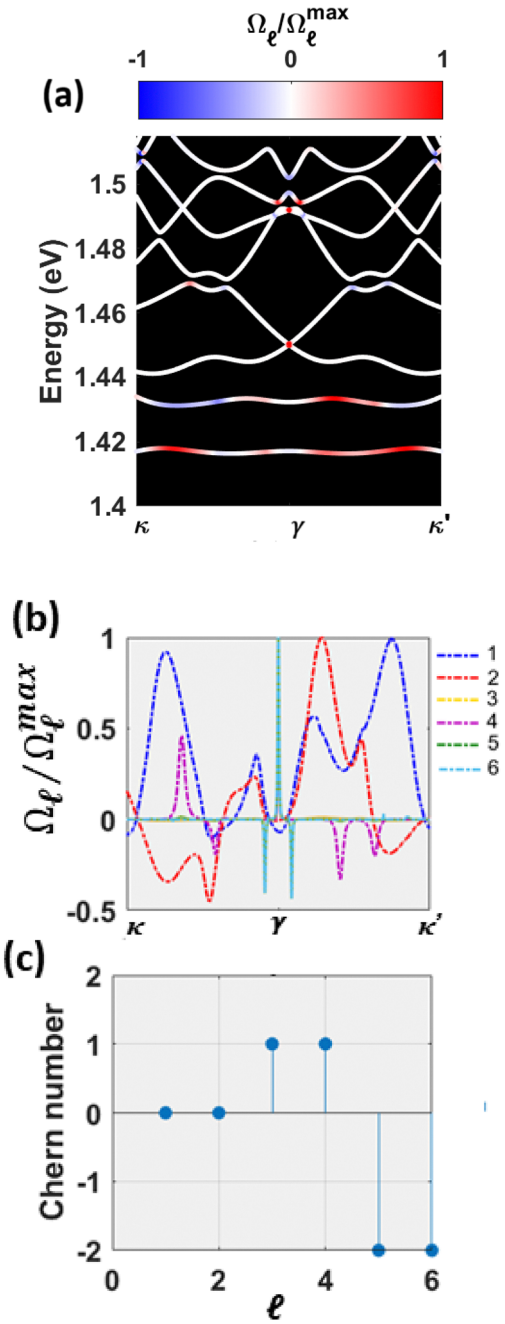

Fig. 5 (a) IX band structure with the projected normalized Berry curvature contribution, computed for a 0.5% normal compressive strain. (b) Normalized Berry curvature distribution over the mBZ for the lowest six bands. Here, the maximum Berry curvature amplitude is on the order of $\Omega^{max} \sim 10^4$ Å^2. (c) Estimated Chern number values for the lowest six bands.

the crucial role of strain orientation in tuning the electronic and optical properties of moiré excitons.

To better understand the impact of heterostrain on the optical properties of moiré excitons, we analyze its effects on the bright-state energies, as shown in Fig. 6. In Fig. 6(a–c), we examine the effects of homogeneous uniaxial, biaxial, and normal compressive strain, respectively. The energies of the bright states exhibit a blueshift under both uniaxial and biaxial strain, revealing an avoided crossing between excited states for small strain strengths ($\varepsilon_s < 1\%$). Notably, in the case of biaxial strain, a quadratic dependence of the bright states' energy is observed for strain strengths exceeding $\varepsilon_s > 1\%$. Interestingly, under normal compressive strain, the bright-state energies redshift for strain strengths below 1%. Around $\varepsilon_s = 1\%$, we observe a butterfly-like behavior characterized by strong coupling between various states. For strain strengths in the range $1\% < \varepsilon_s < 2\%$, the bright-state energies decouple and exhibit a blueshift.

Additionally, we investigate the effects of volume-preserving strain and anisotropic in-plane strain, as shown in Fig. 6(d–f) and (g–k), respectively. Fig. 6(d) corresponds to a strain orientation of $\phi_s = 0^\circ$, which is consistent with the normal compressive strain case in Fig. 6(c). Fig. 6(e) and (f) represent volume-preserving strain with orientations of $\phi_s = 30^\circ$ and $\phi_s = 45^\circ$, respectively. Here, the ground state remains unchanged, satisfying the condition $\mathrm{Tr}(\varepsilon_s) = 0$, which implies that the material's volume and shape are conserved under deformation–a fundamental characteristic of volume-preserving strain. In contrast, the highest excited states shift weakly and exhibit the lifting of degeneracies. Notably, at a strain orientation of $\phi_s = 45^\circ$, correlated states emerge around a strain magnitude of approximately 2%.

For the case of anisotropic in-plane strain, the bright-state energies exhibit a blueshift for strain orientations of $\phi_s = 0^\circ$ and $\phi_s = 45^\circ$, behaving similarly to the uniaxial strain case in Fig. 6(a). However, for $\phi_s = 30^\circ$, the bright-state energies show a redshift, further highlighting the importance of strain orientation for excitonic optical modulator applications.

The strain dependence of the COM's eigenfunctions is also studied in this work. Fig. 7 depicts the first three probability density of states dependence on the biaxial strain for 0.5% and 0.75%, respectively. It's clearly shown that increasing the strain strength gives a rise to three-fold rotation symmetry breaking and thus a mixing between states appearing. This reflects the avoided crossing between bright-state energies in Fig. 6(b), which may lead to an enhancement of optical response in the PL spectra. In Fig. 8, we determine the PL map spectra for moiré IX in a $MoSe_2/WSe_2$ heterobilayer encapsulated in hBN at a 1.35° twist angle under different types of heterostrain. Fig. 8(a)–(c) corresponds to uniaxial, biaxial, and normal compressive strain, respectively. Both uniaxial and biaxial strain lead to an increase in brightness in the ground state, along with enhanced brightness in some excited states. However, in the case of normal compressive strain, we observe an ultra-high PL intensity around 1% strain strength, exhibited by highly correlated excited states.

3.3 Twist and heterostrain interplay modulate layer-hybridized moiré excitons

Our attention now turns to the hybridization phenomena between interlayer and intralayer moiré excitons under the influence of heterostrain. Twist-induced layer-hybridized moiré excitons have been previously observed and effectively described by the hybrid Hamiltonian H_h (eqn (5)). Here, we investigate the degree of hybridization between IX and the intralayer exciton X^{Mo} within the $MoSe_2$ layer under the combined effects of twist and heterostrain. Our analysis reveals the

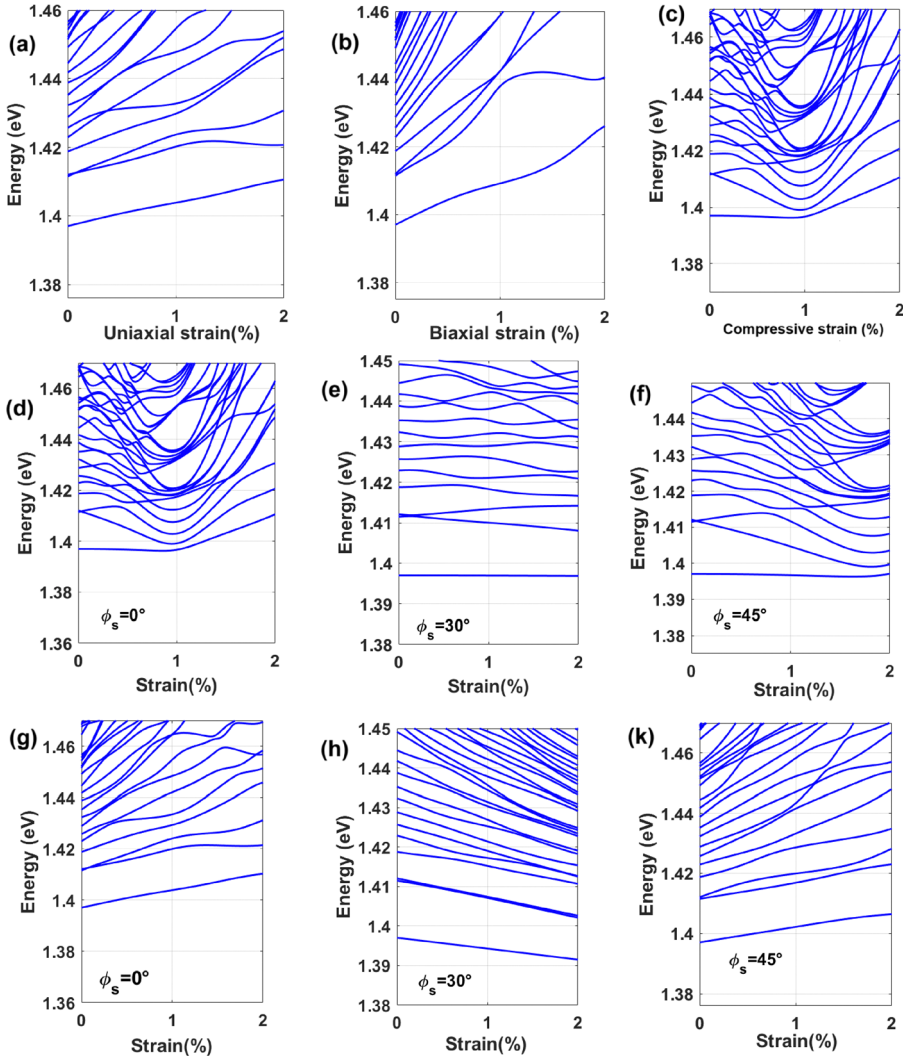

Fig. 6 Strain dependence of IX's bright-state energies around the light cone, at fixed twist-angle θ_t = 1°. (a) and (c) depict the homogeneous uniaxial, biaxial and normal compressive strain dependence, respectively. (d)–(f) The volume-preserving strain dependence, taken for strain direction ϕ_s = 0°, 30° and 45°, respectively. (g)–(k) Anisotropic in-plane strain dependence, taken for ϕ_s = 0°, 30° and 45°, respectively.

intricate interplay between the wavefunctions of these two exciton types, as illustrated in Fig. 1(f).

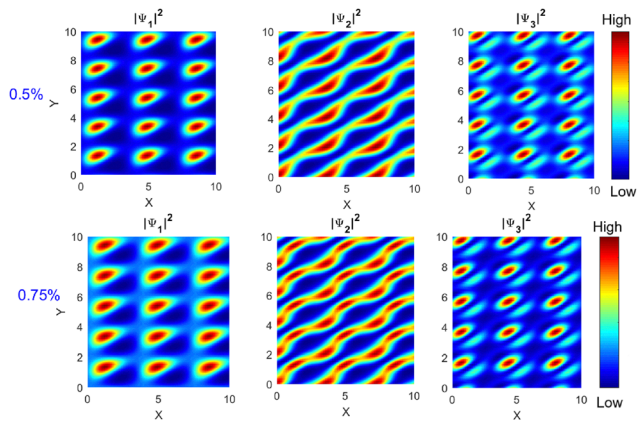

Fig. 7 Biaxial strain tunes the density of states of the first three energy levels.

In Fig. 9, we present the band structure of hybridized moiré excitons under the combined effects of twist and anisotropic in-plane strain, along with excitonic density-projected contributions. Fig. 9(a–d) corresponds to the absence of strain and is computed for different twist angles θ_t = 2°, 3°, 4°, and 5°, respectively. For θ_t = 2°, we observe that the lowest energy states are dominated by the IX density contribution, while hybrid states and states dominated by the intralayer exciton density contribution are situated in the higher excited states. As the twist angle increases, as shown in Fig. 9(b–d), hybrid density contributions begin to emerge in the lowest excited states.

However, the effects of anisotropic in-plane strain are examined in Fig. 9(e–h), for a fixed twist angle of θ_t = 3° and strain orientations ϕ_s = 0° and 10°. Fig. 9(e, f) and (g, h) correspond to strain magnitudes of 1% and 1.5%, respectively. Notably, an intriguing hybrid character is observed in the second-lowest state in Fig. 9(h), further highlighting the importance of the interplay between twist and strain in controlling moiré exciton hybridization.

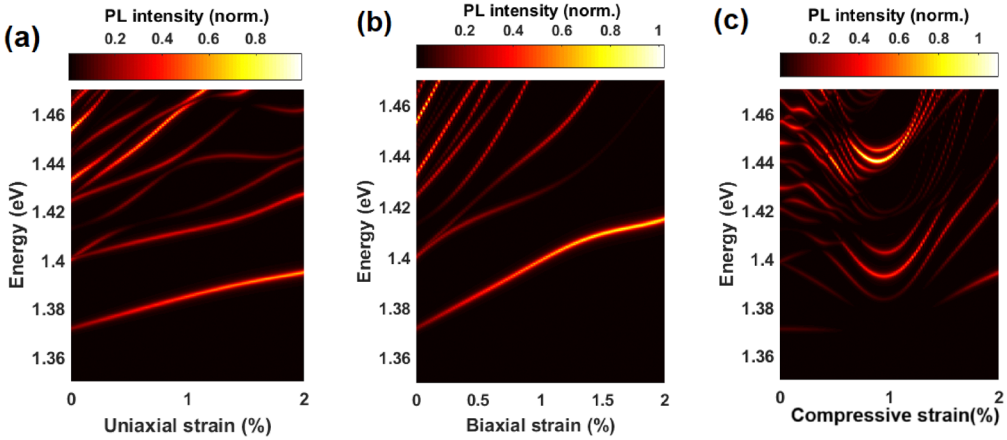

Fig. 8 Moiré IX's PL map dependence on strain effect, for a fixed twist-angle $\theta_t = 1.35°$. (a) Uniaxial strain, (b) biaxial strain and (c) normal compressive strain.

It is worth noting that in our calculations of the density contributions for each part of the exciton, a dominant contribution is identified as either IX or X^{Mo} if the respective density exceeds 90%. Otherwise, the region is classified as a hybrid exciton (hX). These results regarding the hybridization degree controlled by the twist-angle effect can be compared to recent theoretical works based on the continuum model, as reported in ref. 32 and 40. The studied bilayer system is not typically considered an ideal platform for investigating hybrid exciton characteristics at small twist angles, unlike systems such as $WS_2/MoSe_2$[37] and $MoSe_2/MoTe_2$.[41,42] This limitation arises due to the significant internal motion splitting energy between the IX and X^{Mo} in our bilayer system, which are approximately 1.42 eV and 1.56 eV, respectively.

To address this challenge, we varied several experimentally relevant parameters, including the twist angle and strain, to enhance the degree of hybridization within the lowest energy states. Additionally, we propose coupling the 2s Rydberg state of the IX with the 1s Rydberg state of X^{Mo}, which could further enhance the hybridization between these two types of excitons.

4 Conclusion

In this investigation, using a continuum model, we studied moiré excitons in a R-$MoSe_2/WSe_2$ heterobilayer. Experimental parameters, including the twist angle, strain magnitudes, and

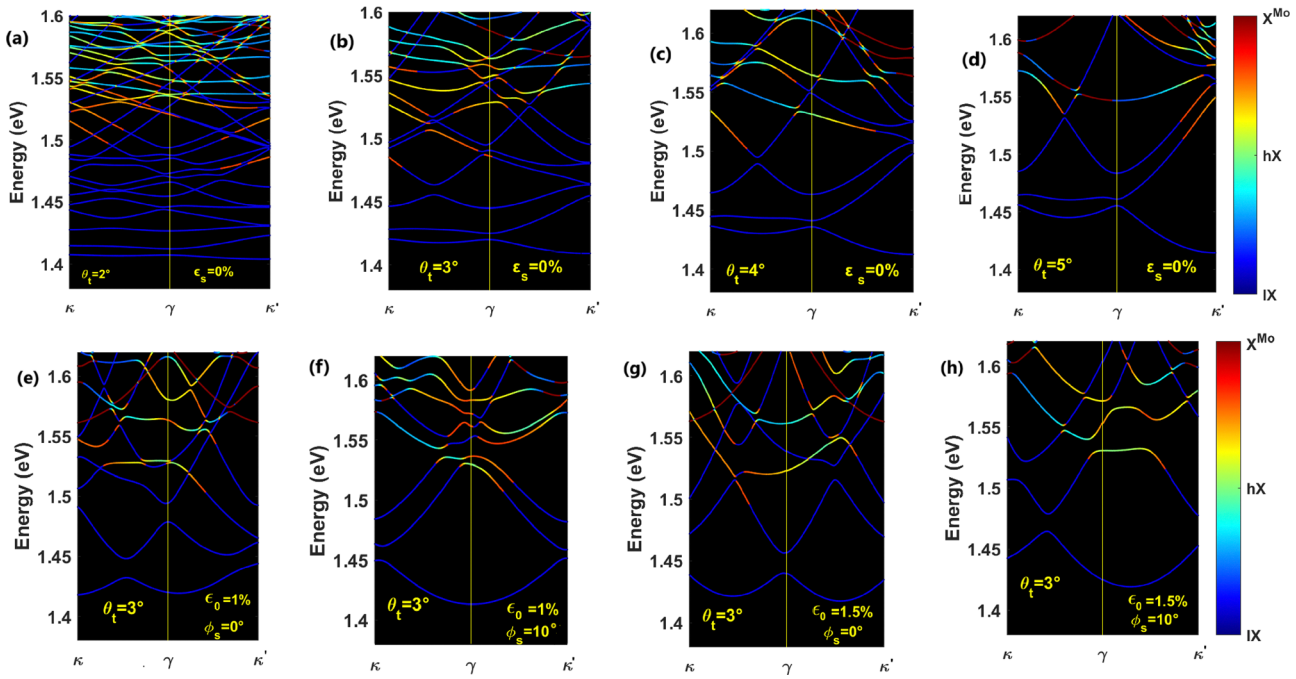

Fig. 9 Twist and strain effect-modulated hybridized moiré exciton band structure with density-projected contributions. In the absence of strain effect (a)–(d), taken for different twist-angles $\theta_t = 2°$, 3°, 4° and 5°, respectively. (e)–(h) Anisotropic in-plane strain effect at fixed twist-angle $\theta_t = 3°$ and strain orientation $\phi_s = 0°$ and 10°, respectively. (e), (f), (g) and (h) correspond to 1% and 1.5% strain magnitude, respectively.

directions, were incorporated to assess their impact on exciton band structures, wavefunction distributions, optical PL spectra, and the degree of hybridization between interlayer and intralayer excitons. The key findings of this study include the demonstration of flat bands exhibited by both interlayer and intralayer excitons in unstrained samples within the weak twist angle regime ($\theta_t < 2^\circ$). We also examined the twist-angle dependence of bright-state energies around the light cone, observing a linear and quadratic increase with respect to the twist angle effect. This behavior is attributed to the presence of a critical twist angle, $\theta_c \simeq 2^\circ$, which separates localized states ($\theta_t < \theta_c$) from delocalized (scattering) states when $\theta_t > \theta_c$. When considering the heterostrain effect, we observed a significant tunability of the moiré exciton band structure and the distribution of bright-state energies. In addition, examining the strain magnitude and direction can enhance the brightness of moiré excitons in the PL spectra. Furthermore, the combined effects of twist and strain result in a high degree of tunability in the hybridization between interlayer and intralayer excitons. Interestingly, for specific strain magnitudes and directions, such as normal compressive strain, we observe the emergence of a topological moiré exciton Chern insulator, characterized by protected edge states. These findings are particularly relevant for potential applications in excitonic optical modulators and the excitonic quantum anomalous Hall effect (EQAHE) enabled by the interplay of twist and strain.

Data availability

The datasets used and/or analyzed during the current study are available from the corresponding author on reasonable request.

Conflicts of interest

There are no conflicts to declare.

Acknowledgements

We are grateful to Prof. Sonia Haddad for the fruitful discussions.

References

1 Z. Li, *et al.*, Efficient strain modulation of 2D materials via polymer encapsulation, *Nat. Commun.*, 2020, **11**, 1151.
2 Z. Liu, *et al.*, Strain and structure heterogeneity in MoS_2 atomic layers grown by chemical vapour deposition, *Nat. Commun.*, 2014, **5**, 5246.
3 A. Kumar, *et al.*, Strain fingerprinting of exciton valley character, *Nat. Commun.*, 2024, **15**, 7546.
4 P. H. López, *et al.*, Strain control of hybridization between dark and localized excitons in a 2D semiconductor, *Nat. Commun.*, 2022, **13**, 7691.
5 S. Pac, *et al.*, Strain-mediated interlayer coupling effects on the excitonic behaviors in an epitaxially-grown MoS_2/WS_2 van der Waals heterobilayer, *Nano Lett.*, 2017, **17**(9), 5634–5640.
6 Q. Tong, H. Yu, Q. Zhu, Y. Wang, X. Xu and W. Yao, Topological mosaics in moiré superlattices of van der Waals heterobilayers, *Nat. Phys.*, 2017, **13**, 356–362.
7 F. Carrascoso, D.-Y. Lin, R. Frisenda and A. Castellanos-Gomez, Biaxial strain tuning of interlayer excitons in bilayer MoS2, *JPhys Mater.*, 2020, **3**, 015003.
8 Z. Bi, N. F. Q. Yuan and L. Fu, Designing flat bands by strain, *Phys. Rev. B*, 2019, **100**, 035448.
9 C. Si, Z. Suna and F. Liu, Strain engineering of graphene: a review, *Nanoscale*, 2016, **8**, 3207–3217.
10 P. Shi, Y. Chen, J. Feng and P. Sareh, Highly stretchable graphene kirigami with tunable mechanical properties, *Phys. Rev. E*, 2024, **109**, 035002.
11 M. Mannaï and S. Haddad, Twistronics versus straintronics in twisted bilayers of graphene and transition metal dichalcogenides, *Phys. Rev. B*, 2021, **103**, L201112.
12 M. Mannaï and S. Haddad, Strain tuned topology in the Haldane and the modified Haldane models, *J. Phys.: Condens. Matter*, 2020, **32**, 225501.
13 J.-X. Hu, C.-P. Zhang, Y.-M. Xie and K. T. Law, Nonlinear Hall effects in strained twisted bilayer WSe_2, *Commun. Phys.*, 2022, **5**, 255.
14 D.-N. Liu and Y. Guo, Strain-tuned spin polarization and optical conductivity in MoS_2/EuS heterostructures, *Phys. Rev. B*, 2023, **107**, 075430.
15 S. Zhu and H. T. Johnson, Moiré-templated strain patterning in transition metal dichalcogenides and application in twisted bilayer MoS_2, *Nanoscale*, 2018, **10**, 20689.
16 E. Blundo, *et al.*, Strain-Induced Exciton Hybridization in WS_2 Monolayers Unveiled by Zeeman-Splitting Measurements, *Phys. Rev. Lett.*, 2022, **129**, 067402.
17 B. Aslan, M. Deng and T. F. Heinz, Strain tuning of excitons in monolayer WSe_2, *Phys. Rev. B*, 2018, **98**, 115308.
18 R. Amairi, A. Smiri and S. Jaziri, Layer-number and strain effects on the structural and electronic properties of PtSe2 material, *J. Phys.:Condens. Matter*, 2025, **37**, 035501.
19 D. Zhai and W. Yao, Theory of tunable flux lattices in the homobilayer moiré of twisted and uniformly strained transition metal dichalcogenides, *Phys. Rev. Mater.*, 2020, **4**, 094002.
20 H. Yu, M. Chen and W. Yao, Giant magnetic field from moire induced Berry phase in homobilayer semiconductors, *Natl. Sci. Rev.*, 2020, **7**, 12.
21 H. Zheng, D. Zhai and W. Yao, Twist versus heterostrain control of optical properties of moiré exciton minibands, *2D Mater.*, 2021, **8**, 044016.
22 H. Yu, G.-B. Liu, J. Tang, X. Xu and W. Yao, Moiré excitons: From programmable quantum emitter arrays to spin-orbit-coupled artificial lattices, *Sci. Adv.*, 2017, **3**, e1701696.
23 Y. Bi, *et al.*, Excitons in strain-induced one-dimensional moiré potentials at transition metal dichalcogenide heterojunctions, *Nat. Mater.*, 2020, **19**, 1068–1073.
24 I. Niehues, *et al.*, Interlayer excitons in bilayer MoS_2 under uniaxial tensile strain, *Nanoscale*, 2019, **11**, 12788.

25 M. Richter, Theory of interlayer exciton dynamics in two-dimensional transition metal dichalcogenide heterolayers under the influence of strain reconstruction and disorder, *Phys. Rev. B*, 2024, **109**, 125308.
26 S. Deng, Yi Chu and Q. Zhu, Moiré exciton condensate: Nonlinear Dirac point, broken-symmetry Bloch waves, and unusual optical selection rules, *Phys. Rev B*, 2022, **106**, 155410.
27 H. Guo, X. Zhang and G. Lu, Tuning moiré excitons in Janus heterobilayers for high-temperature Bose–Einstein condensation, *Sci. Adv.*, 2022, **8**, eabp9757.
28 H.-Y. Xie, P. Ghaemi, M. Mitranoc and B. Uchoa, Theory of topological exciton insulators and condensates in flat Chern bands, *Proc. Natl. Acad. Sci. U. S. A.*, 2024, **121**, e2401644121.
29 Y. Cao, *et al.*, Unconventional superconductivity in magic-angle graphene superlattices, *Nature*, 2018, **556**, 43–50.
30 H. Isobe, N. F. Q. Yuan and L. Fu, waves in twisted bilayer graphene, *Phys. Rev. X*, 2018, **8**, 041041.
31 X. Lu, *et al.*, Superconductors, orbital magnets and correlated states in magicangle bilayer graphene, *Nature*, 2019, **574**, 653–657.
32 M. Xie, M. Hafezi and S. D. Sarma, Long-lived Topological Flatband Excitons in Semiconductor Moiré Heterostructures: A Bosonic Kane-Mele Model Platform, *Phys. Rev. Lett.*, 2024, **133**, 136403.
33 Y.-W. Chang, Continuum model study of optical absorption by hybridized moiré excitons in transition metal dichalcogenide heterobilayers, *Phys. Rev. B*, 2023, **108**, 155424.
34 A. Julku, Nonlocal interactions and supersolidity of moiré excitons, *Phys. Rev. B*, 2022, **106**, 035406.
35 Y. Tang, *et al.*, Tuning layer-hybridized moiré excitons by the quantum-confined Stark effect, *Nat. Nanotechnol.*, 2021, **16**, 52–57.
36 F. Tagarelli, *et al.*, Electrical control of hybrid exciton transport in a van der Waals heterostructure, *Nat. Photonics*, 2023, **17**, 615–621.
37 E. M. Alexeev, *et al.*, Resonantly hybridized excitons in moiré superlattices in van der Waals heterostructures, *Nature*, 2019, **567**, 81–86.
38 S. Brem, *et al.*, Hybridized intervalley moiré excitons and flat bands in twisted WSe_2 bilayers, *Nanoscale*, 2020, **12**, 11088.
39 C. Jin, *et al.*, Observation of moiré excitons in WSe_2/WS_2 heterostructure superlattices, *Nature*, 2019, **567**, 76–80.
40 K. W. Song and O. Kyriienko, Electrically Tunable and Enhanced Nonlinearity of Moiré Exciton-Polaritons in Transition Metal Dichalcogenide Bilayers, arXiv, 2024, preprint, arxiv:2406.08263v1.
41 D. A. Ruiz-Tijerina and V. I. Falko, Interlayer hybridization and moiré superlattice minibands for electrons and excitons in heterobilayers of transition-metal dichalcogenides, *Phys. Rev. B*, 2019, **99**, 125424.
42 S. Zhao, *et al.*, Hybrid Moiré Excitons and Trions in Twisted $MoTe_2$−$MoSe_2$ Heterobilayers, *Nano Lett.*, 2024, **24**, 4917–4923.
43 B. Polovnikov, *et al.*, Field-induced hybridization of moiré excitons in $MoSe_2/WS_2$ heterobilayers, *Phys. Rev. Lett.*, 2024, **132**, 076902.
44 S. Brem, C. Linderalv, P. Erhart and E. Malic, Tunable Phases of Moiré Excitons in van der Waals Heterostructures, *Nano Lett.*, 2020, **20**, 8534–8540.
45 J. M. Fitzgerald, J. J. P. Thompson and E. Malic, Twist Angle Tuning of Moiré Exciton Polaritons in van der Waals Heterostructures, *Nano Lett.*, 2022, **22**, 4468–4474.
46 D. A. Ruiz-Tijerina, I. Soltero and F. Mireles, Theory of moiré localized excitons in transition metal dichalcogenide heterobilayers, *Phys. Rev. B*, 2020, **102**, 195403.
47 D. Chen, *et al.*, Tuning moiré excitons and correlated electronic states through layer degree of freedom, *Nat. Commun.*, 2022, **13**, 4810.
48 F. Wu, T. Lovorn and A. H. MacDonald, Theory of optical absorption by interlayer excitons in transition metal dichalcogenide heterobilayers, *Phys. Rev. B*, 2018, **97**, 035306.
49 F. Wu, T. Lovorn and A. H. Mac Donald, Topological Exciton Bands in Moiré Heterojunctions, *Phys. Rev. Lett.*, 2017, **118**, 147401.
50 E. Liu, *et al.*, Signatures of moiré trions in $WSe_2/MoSe_2$ heterobilayers, *Nature*, 2021, **594**, 46–50.
51 J. P. Bange, *et al.*, Ultrafast dynamics of bright and dark excitons in monolayer WSe_2 and heterobilayer WSe_2/MoS_2, *2D Mater.*, 2023, **10**, 035039.
52 N. S. Rytova, Screened potential of a point charge in a thin film, Proc. MSU Phys., Astron, 1967, **3**, 30.
53 L. V. Keldysh, Coulomb interaction in thin semiconductor and semimetal films, *J. Exp. Theor. Phys.*, 1979, **29**, 658.
54 H. E. Hannachi and S. Jaziri, Stark effect and orbital hybridization of moiré interlayer excitons in the $MoSe_2/WSe_2$ heterobilayer, *Phys. Chem. Chem. Phys.*, 2024, **26**, 21753–21766.
55 H. E. Hannachi, M. O. Goerbig and S. Jaziri, Berry curvature contribution towards 1s-2p interlayer exciton ultrafast transition within a R-$WSe_2/MoSe_2$ heterobilayer, arXiv, 2024, preprint, arxiv:2408.04136v1.
56 H. E. Hannachi, D. Elmaghraoui and S. Jaziri, Moiré interlayer exciton relative and center of mass motions coupling, Effect on 1s-np interlayer exciton THz transitions, *Eur. Phys. J. Plus*, 2023, **138**, 396.
57 J. Kang, S. Tongay, J. Zhou, J. Li and J. Wu, Band offsets and heterostructures of two-dimensional semiconductors, *Appl. Phys. Lett.*, 2013, **102**, 012111.
58 S. Conti, *et al.*, Flattening conduction and valence bands for interlayer excitons in a moiré MoS_2/WSe_2 heterobilayer, *Nanoscale*, 2023, **15**, 14032.
59 R. Bhattarai, P. Minch, Y. Liang, S. Zhang and T. D. Rhone, Strain-induced topological phase transition in ferromagnetic Janus monolayer $MnSbBiS_2Te_2$, *Phys. Chem. Chem. Phys.*, 2024, **26**, 10111.